JGR Solid Earth

RESEARCH ARTICLE

10.1029/2019JB018888

Key Points:

- Altered basalt exhibits velocity weakening behavior at the updip limit of the seismogenic zone ($T = 150$ °C)
- Altered basalt may be a preferential host for earthquake nucleation in this environment
- Mixing altered basalt with shale may be a mechanism for producing shallow slow earthquake phenomena

Supporting Information:

- Supporting Information S1
- Table S1

Correspondence to:
N. J. Phillips,
noah.phillips@mail.mcgill.ca

Citation:
Phillips, N. J., Belzer, B., French, M. E., Rowe, C. D., & Ujiie, K. (2020). Frictional strengths of subduction thrust rocks in the region of shallow slow earthquakes. *Journal of Geophysical Research: Solid Earth*, *125*, e2019JB018888. https://doi.org/10.1029/2019JB018888

Received 12 OCT 2019
Accepted 30 JAN 2020
Accepted article online 3 FEB 2020

Frictional Strengths of Subduction Thrust Rocks in the Region of Shallow Slow Earthquakes

Noah John Phillips[1], **Ben Belzer**[2], **Melodie E. French**[2], **Christie D. Rowe**[1], and **Kohtaro Ujiie**[3]

[1]Department of Earth and Planetary Sciences, McGill University, Montreal, Quebec, Canada, [2]Department of Earth, Environmental and Planetary Sciences, William Marsh Rice University, Houston, TX, USA, [3]Graduate School of Life and Environmental Sciences, University of Tsukuba, Tsukuba, Japan

Abstract Earthquakes are expected to nucleate within velocity-weakening materials; however, at the updip limit of the subduction seismogenic zone, the principal lithologies exhibit velocity-strengthening behavior. At an exhumed analogue for present-day subduction at Nankai (the Mugi Mélange, Japan) two examples of paleoseismic features occur within altered basalts, suggesting that they may be velocity-weakening. We shear altered basalt and shale matrix from the mélange in the triaxial saw cut configuration at in situ conditions of deformation ($P_c = 120$ MPa, $T = 150$ °C) for two pore fluid factors ($\lambda = 0.36, 0.7$). The shale matrix exhibits a coefficient of friction between 0.4 and 0.5, and velocity-strengthening behavior. Altered basalt exhibits Byerlee friction and velocity-weakening behavior. In most experiments deformation was partitioned into Riedel shears, which have a lower percentage of clasts, clast size distributions with higher fractal dimensions, and shape factors indicating rounder clasts compared to the matrix between Riedel shears. We hypothesize that earthquakes preferentially nucleate within altered basalt at the updip limit of the seismogenic zone. More complex forms of deformation (e.g., shallow very low frequency earthquakes) may occur by mixing velocity-weakening altered basalt into the velocity-strengthening shale matrix. In subduction zones where the matrix is composed of shale, this complex behavior is limited to shallow depths ($T < \sim 250$ °C), above the updip transition to velocity-weakening behavior for the matrix. Altered basalt is a ubiquitous subducting material, and future studies on its behavior through a range of subduction zone conditions are required for a full understanding of the mechanical behavior of subduction zones.

1. Introduction

Understanding the mechanics of slip in subduction zones is important for models of the earthquake cycle (Wang et al., 2012). Depth-related changes in the locked or creeping state of the subduction plate boundary are revealed by seismicity patterns, and geodetic detection of strain and slip (e.g., Avouac, 2015; Bilek & Lay, 1999; Mavrommatis et al., 2014). Between locked and creeping portions of the subduction plate boundary is a transitional zone where slow slip events, tremor, and low frequency earthquakes, collectively known as slow earthquake phenomena, frequently occur (Beroza & Ide, 2011; Bürgmann, 2018; Obara, 2002; Rogers & Dragert, 2003; Shelly et al., 2007). Observations of slow slip phenomena are more abundant from the downdip limit of the seismogenic zone where land-based seismic and geodetic networks have better resolution, but advanced processing methods and increasing ocean-bottom instrumentation has revealed similar events at the updip limit (Figure 1; e.g., Obana & Kodaira, 2009; Saffer & Wallace, 2015; Araki et al., 2017; Mcguire et al., 2018; Nakano et al., 2018). The predominant slip behavior at a given depth (i.e., earthquakes, slow slip, fault creep) is controlled by the frictional properties of subducting materials (Ikari et al., 2018; Saffer & Marone, 2003; Scholz, 1998), particularly in the shallow portion of subduction zones where dislocation- and diffusion-creep are unlikely to occur due to low temperatures (Kohlstedt et al., 1995). Understanding the frictional properties of units typical of shallow subduction zones is therefore important for understanding the complex slip behavior of these environments.

Exhumed subduction zone fault rocks preserve information about the composition, structure, and behavior of the subduction plate boundary (Fagereng, 2011; Kimura et al., 2012; Rowe et al., 2005). Creep, slow slip, and seismic propagation in the shallow portion of the subduction thrust are both controlled by, and recorded by, these rocks, which are commonly represented in ancient accretionary complexes as tectonic mélanges

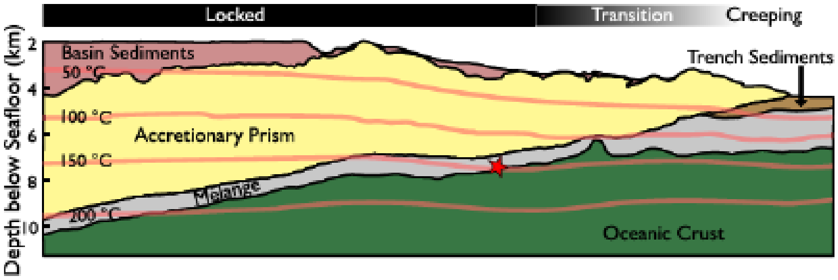

Figure 1. Geotectonic setting of the studied samples. Cross section of the Nankai subduction zone (offshore Kumano) based on seismic reflection data (Moore et al., 2009) with overlain geothermal gradients (Harris et al., 2011, their Model B). Studied samples come from the Mugi Mélange, a Late Cretaceous analogue for the Nankai trough that has been exhumed to the surface. Red star indicates the equivalent position of underplating of the Mugi Mélange samples. Black bar shows the transition from locked to creeping behavior along the plate interface.

(Cowan, 1985; Kimura et al., 2012). Tectonic mélanges are produced by distributed shear within downgoing sediments above the oceanic plate (Fagereng, 2011; Fisher & Byrne, 1987; Hashimoto & Kimura, 1999; Kimura et al., 2012; Kitamura et al., 2005; Moore, 1989). Basaltic slabs (incorporated into the sediments through underplating) and sandstone layers form boudins within a shale dominated matrix due to viscosity contrasts within these zones of distributed shear (Fagereng & Sibson, 2010; Kimura et al., 2012).

Within the Mugi Mélange, Japan, evidence of paleoseismicity is present along the upper contact of the shale matrix mélange (against coherent offscraped quartz-rich turbidite sequences), and within the center of the mélange along the contacts of incorporated basaltic slabs (Kameda et al., 2011; Phillips et al., 2019; Ujiie, Yamaguchi, Sakaguchi, & Toh, 2007), which have been altered to a mixture of chlorite and albite (Ujiie, Yamaguchi, Kimura, & Toh, 2007; Phillips et al., 2019). In this paper, we examine the frictional properties of the subducting sediment and altered basalt from Mugi, which serves as an on-land analogue for the Nankai trough (Figure 1). The experiments in this paper measure the frictional properties of these materials to explain why altered basaltic samples host seismic features, and to evaluate potential explanations for some of the more complex styles of slip and seismic behaviors found in shallow subduction zones. Experiments were performed at the in situ temperatures and pressures of deformation, and explored the range of pore fluid factors observed for the Nankai trough (Kitajima & Saffer, 2012; Tonegawa et al., 2017). We use microstructural observations of experimentally deformed samples to explain the velocity-dependent frictional behavior of experiments, and compare them with additional microstructural observations of natural faults in the Mugi Mélange to interpret its deformation history.

2. Materials and Methods

2.1. Samples

Natural subduction zone samples were collected from the upper Mugi Mélange, part of the Late Cretaceous Shimanto Accretionary Complex in Japan (Kimura et al., 2012; Kitamura et al., 2005). The mélange is widely recognized as an on-land analogue for present-day subduction at Nankai (Ujiie & Kimura, 2014), and is composed of a stack of thrust imbricates (Shibata et al., 2008). Each thrust stack has a similar internal stratigraphy: at the base is a 10–30-m-thick layer of basalt (interpreted to be underplated oceanic plate) which is overlain by a mélange with a shale matrix containing blocks of sandstone and basalt, and discontinuous layers of volcanic tuff (Kitamura et al., 2005; Shibata et al., 2008). The margins of basaltic layers and blocks have been predominantly altered to a mixture of plagioclase and chlorite. Altered basalt occurs as ~60-cm-thick rims around basaltic blocks and layers (Phillips et al., 2019). The evidence for localized slip is concentrated within altered basalt, along/near interfaces with shale matrix so the properties of these two lithologies are important for understanding the frictional behavior of these mélanges.

Microstructures of the shale matrix show evidence for distributed deformation, with development of a strong foliation defined by aligned phyllosilicates, clasts of sandstone, and pressure solution seams (Kitamura et al., 2005; Kawabata et al., 2007; Figure 2a). Microstructures in the altered basalt show evidence of localized deformation, with well-developed cataclasites tens of centimeters thick and thin through-going faults

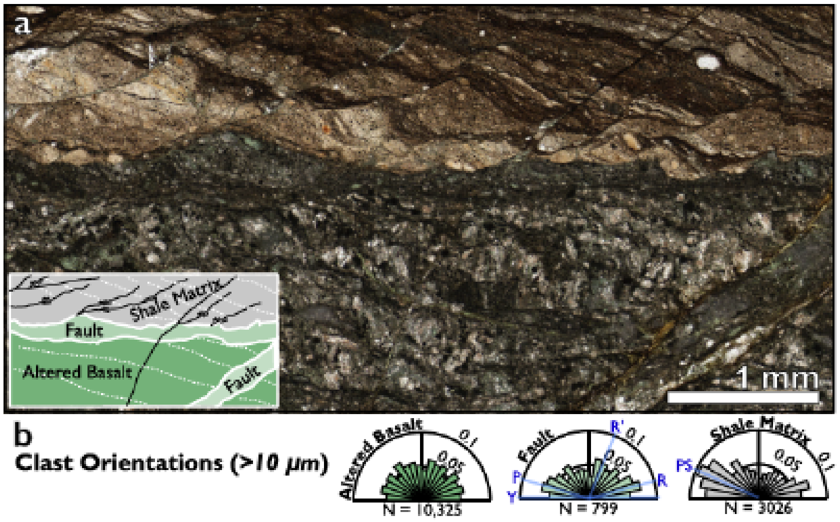

Figure 2. (a) Typical microstructure from the interface between altered basalt and shale matrix. Shale matrix shows a strong foliation, while localized faults cut the altered basalt along the interface. (b) Orientations of clasts (showing the distribution of Feret angles as probability density functions) from each microstructural domain using the grain shape analysis outlined in section 2.5 (note that only the horizontal fault was used for "fault"; reflected light image and images of segregated clasts for each domain are found in Figure S3). Average Riedel shear orientations from Logan et al. (1992) are labeled for the fault, and the orientation of the foliation (PS) is labeled for the shale matrix.

cutting the altered basaltic unit (Phillips et al., 2019; Figure 2a). The unaltered basalts show little internal deformation. We sampled and performed friction experiments on both the shale from the mélange matrix and the altered basalt from the margin of a basaltic layer to test their frictional properties at in situ conditions. For comparison, microstructural analyses were conducted on both experimental and naturally deformed samples from the shale mélange matrix and the altered basalt, as well as a fault that cross-cuts the altered basalt.

2.2. X-ray Diffraction

The compositions of the starting materials were analyzed using X-ray diffraction at McGill University. Samples were crushed by hand in 30-s intervals to <0.5 mm (with sieving between each interval) and were subsequently crushed for 2 min using a McCrone Mill. Both random powders and oriented clay separates were prepared (following Poppe et al., 2001) and analyzed. Random powders were back-packed into a sample holder with a glass backing. Random powders were run between 2 and 70° 2θ (Figure 3). Oriented clay separates were run dry and glycolated between 2 and 40° 2θ. All runs used a scan speed of 1° per minute, and a scan step of 0.01°. Reitveld analysis of the random powder analyses was performed using the software PDXL 2 (Rigaku).

2.3. Experimental Setup and Procedure

Experiments were performed using a triaxial deformation apparatus housed at Rice University (Figure 4a). Samples were deformed between steel forcing blocks in the saw cut geometry. The apparatus uses silicon oil as a confining medium and is equipped with servo-controlled intensifiers to control both confining and pore fluid pressures. External heating bands heat the assembly to a maximum temperature of 200 °C, and an internal thermocouple measures the temperature near the sample. Axial displacement imposed by a servo-controlled hydraulic piston causes shear displacement along the 35° saw cut. Axial displacement is measured using a linear variable differential transformer above the upper piston, and displacement is corrected for elastic distortion of the apparatus using a calibrated stiffness of 2.5×10^8 N/m. An internal load cell measures the axial force applied to the sample (Figure 4a). We convert axial force, confining pressure, and pore pressure to shear stress and effective normal stress along the saw cut following standard procedures, including corrections for the change in surface area with shear strain, elasticity of the deformation apparatus, and jacket strength (e.g., Chester & Higgs, 1992; Marone et al., 1990; Tembe et al., 2010). Consistent with previous studies of gouge strength, we report the strength as the friction coefficient

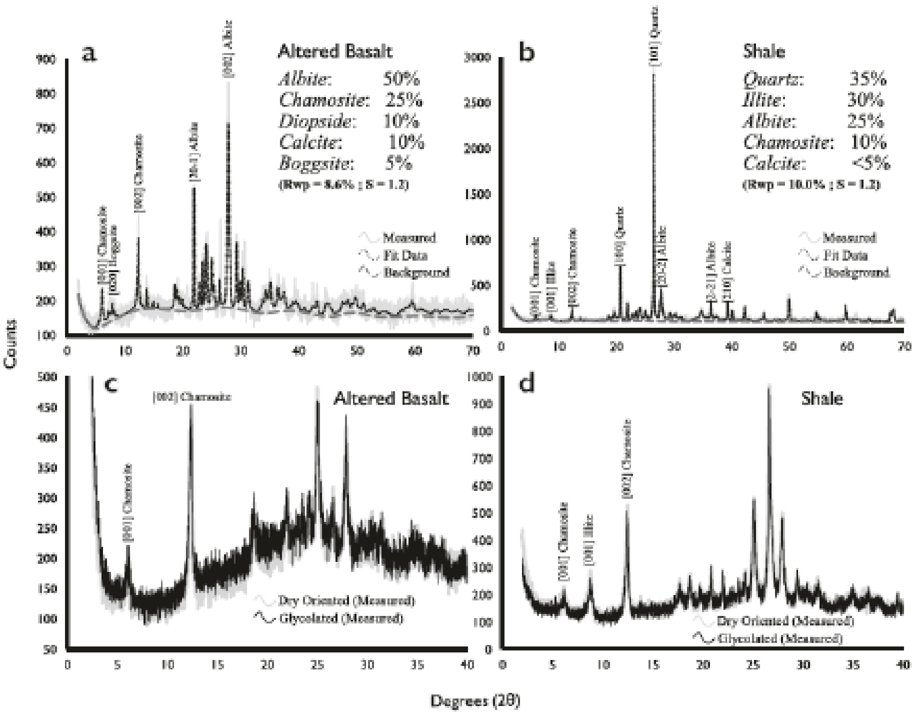

Figure 3. X-ray diffraction patterns of the main lithologies examined in this paper. (a and b) Measured, fit, and background obtained from randomly oriented, backpacked mounts. Reitveld results (rounded to the nearest 5%) are shown. (c and d) Analysis of dry-oriented and glycolated clay aggregates. No expansion was observed in the clay separates following glycolation.

(shear stress/normal stress − pore pressure) and ignore cohesion (e.g., Chester & Higgs, 1992 ; Marone, 1998). For these experiments, samples were double jacketed in 0.5-mm-thick Teflon heat-shrink tubes, and the measured axial force was corrected for the strength of Teflon using the data of Coble et al. (2014). We assume that the rate-dependent strength of the Teflon is negligible compared to the response of the sample.

To prepare samples for deformation experiments and to simulate gouges observed in natural faults, samples were disaggregated to particles <125 μm in diameter using a mortar and pestle. Samples were crushed in 30-s intervals and were sieved between each interval to remove the <125-μm fraction. The >125-μm fraction was returned to the mortar and pestle and the process was repeated until the sample was completely disaggregated. Samples were prepared by mixing 3.5 g of powder with deionized water to form a thick paste, which was applied to the forcing blocks to form a 2-mm-thick layer. Once the samples were jacketed and placed in the pressure vessel, confining and pore fluid pressures were increased linearly and simultaneously to maintain a constant pore fluid factor, λ (ratio of pore fluid pressure to least compressive stress), of either 0.36 or 0.7. This procedure avoids overconsolidation of the gouge. The experimental setup then equilibrated at the experimental pore fluid and confining pressures for 8–12 hr while the vessel and sample assembly heated overnight, which allowed the gouge samples to compact before starting the experiment and for the fluid pressures to equilibrate across the layer of gouge.

Three sets of experiments were conducted on altered basalt and shale samples (Table 1). All experiments were run at a confining pressure of 120 MPa and a temperature of 150 °C; these conditions are in the range of estimated deformation temperatures for the Mugi Mélange (Ikesawa et al., 2005) and also reflect the conditions of the plate interface at the NanTroSEIZE site (Harris et al., 2011; Sugihara et al., 2014). Pore fluid factors (0.36 and 0.7) were selected based on estimates of pore fluid pressures from shear wave velocities (Tonegawa et al., 2017) and *P*-wave velocities (Kitajima & Saffer, 2012) from Nankai. Low-velocity zones, which overlap with epicenters for shallow low frequency earthquakes, have estimated pore fluid factors of ~0.7 while elsewhere in Nankai pore fluid factors range from 0.35 to 0.5 (Kitajima & Saffer, 2012; Tonegawa et al., 2017).

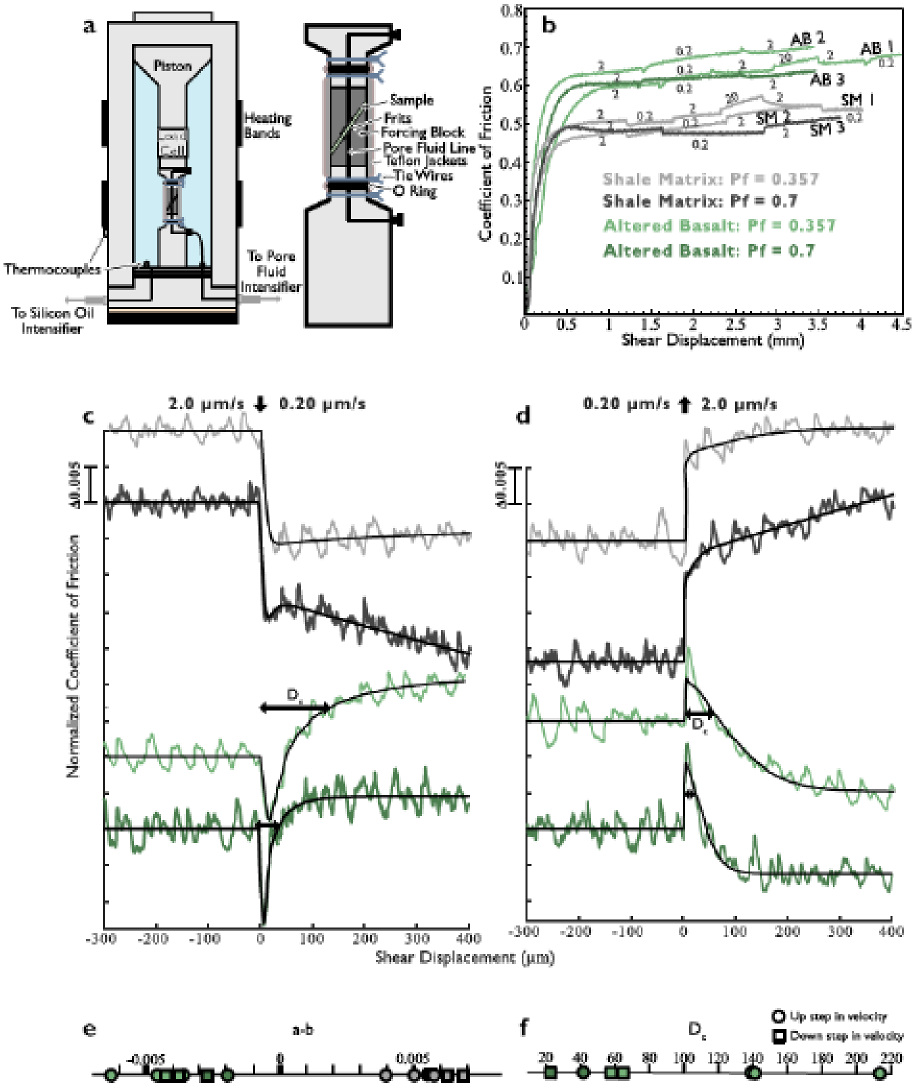

Figure 4. Experimental configuration and results. (a) Schematic of the triaxial apparatus housed at Rice University. (b) Results of friction experiments on crushed altered basalt (AB) and shale matrix (SM). Labeled shear velocities are in μm/s. (c) Model results of rate-steps from shear velocities of 2.0 to 0.20 μm/s and (d) for rate-steps from 0.20 to 2.0 μm/s. Displacements are offset so that 0 μm is the location of the rate-steps. Widths of double-headed arrows indicate the modeled critical slip distances (D_c) for altered basalt. (e) Fits for *a-b* from all experiments for rate-steps between 0.20 and 2.0 μm/s. (f) Fits of the critical slip distance (D_c) from experiments on altered basalt for rate-steps between 0.20 and 2.0 μm/s. (Fits for the shale matrix are not included due to the high errors associated with the negligible evolutionary effect.) For both (e) and (f), circles show upsteps in velocity, squares depict downsteps, and the color of the fill matches experiments presented in (b).

In experimental set 1, altered basalt and shale samples were deformed at a pore fluid factor of 0.36 and five rate steps were imposed at shear velocities between 0.20 and 20 μm/s to evaluate the rate-and-state frictional properties of the samples at in situ conditions of deformation (Table 1). Experiments from sets 2 and 3 were conducted at pore fluid factors of 0.36 and 0.7, respectively, included only two rate steps at shear velocities between 0.20 and 2.0 μm/s, and were used for microstructural analysis (Table 1). Experiments are labelled in this paper by sample type and set number (e.g., AB2 = Altered basalt, Set 2).

At the fastest shear velocities, the pore fluids may become undrained (e.g., the pore fluid pressure in the gouge may be greater than the imposed pore fluid pressure due to compaction and slow equilibration of pore waters). Following Faulkner et al. (2017) and Xing et al. (2019) we calculate the time (*t*) for fluid in the gouge to equilibrate following a rate step, where

Table 1
Experimental Conditions

Name	λ	Rate stepping sequence (μm/s)	P_c (MPa)	T (°C)	sd (mm)	Microstructures
AB1	0.357	2.0–0.20–2.0–20–2.0–0.20	120	150	4.5	No
AB2	0.357	2.0–0.20–2.0	120	150	3.4	Yes
AB3	0.7	2.0–0.20–2.0	120	150	3.5	Yes
SM1	0.357	2.0–0.20–2.0–20–2.0–0.20	120	150	4.4	No
SM2	0.357	2.0–0.20–2.0	120	150	3.3	Yes
SM3	0.7	2.0–0.20–2.0	120	150	3.7	Yes

Note. λ = pore fluid factor, P_c = confining pressure, T = temperature, sd = total shear displacement.

$$t = \frac{h^2\beta\eta}{2k} \tag{1}$$

where h is the diffusion length (equal to 0.002 m of gouge thickness), β is the compressibility of the gouge (~10^{-10} Pa^{-1} following Faulkner et al. (2017)), η is the viscosity of the fluid (0.001 Pa s for water), and k is the permeability of the gouge (~10^{-20} s^{-1} following Faulkner et al. (2017)). Using these estimated parameters, it takes ~20 s for the pore fluids to equilibrate following a rate step, indicating that our fastest rate steps are likely undrained and may experience elevated fluid pressures.

After equilibrating overnight, samples were sheared at 2.0 μm/s to a shear displacement between 1.20 and 1.75 mm. Once a steady state coefficient of friction was reached, the first velocity-step was applied to the samples, and for experiments from set 1, subsequent rate-steps were applied once the sample appeared to achieve a new steady state (Figure 4b). An exception to this was for rate-steps to 20 μm/s. During these velocity steps the sample exhibited strain hardening at a faster rate than during other velocity steps, and did not achieve a new steady state (Figure 4b). As such, rate steps between 2.0 and 20 μm/s were not used to fit rate-and-state parameters. For experiments from sets 2 and 3, a single set of rate-steps were applied (decrease to 0.20 μm/s, increase to 2.0 μm/s), with 1–2 mm of shear displacement following each step.

2.4. Rate-and-State Fitting

The experimentally determined shear stresses (τ), normal stresses (σ_n), and pore fluid pressures (P_f) were used to calculate the friction coefficient (μ) during experiments, where

$$\mu = \frac{\tau}{\sigma_n - P_f}. \tag{2}$$

To determine the velocity dependence of friction, data were fit with the rate-and-state friction relation using an iterative least squares inversion method (Reinen & Weeks, 1993) and the RS3000 code developed for triaxial deformation apparatus (Skarbek & Savage, 2019). Individual rate-steps were de-trended using a linear fit to the 300 μm before the rate-step to correct for slip hardening, and the 400 μm following each rate-step was used to model the evolution of friction. The evolution of friction (μ) following rate-steps was fit using one or two state variables (θ; two state variables was only used for sample SM3; see Table S1) and both the aging (Dieterich) and slip (Ruina) laws for state variable evolution (Dieterich, 1978; Marone, 1998; Ruina, 1983). In the rate-and-state formulation, friction is described by

$$\mu = \mu_0 + a\ln\left(\frac{V}{V_0}\right) + b\left(\frac{V_0\theta}{D_c}\right) \tag{3}$$

where V_0 and V are the reference and current velocities, respectively, μ_0 is the coefficient of friction at V_0, D_c is the critical slip distance, and a and b are the empirical constants describing the magnitude of the change in μ following a rate-step and the magnitude of the change during its subsequent evolution back to a new steady state, respectively. The state variable (θ) is either described by the aging law (Dieterich, 1978)

$$\frac{d\theta}{dt} = 1 - \frac{V\theta}{D_c} \tag{4}$$

or the slip law (Ruina, 1983)

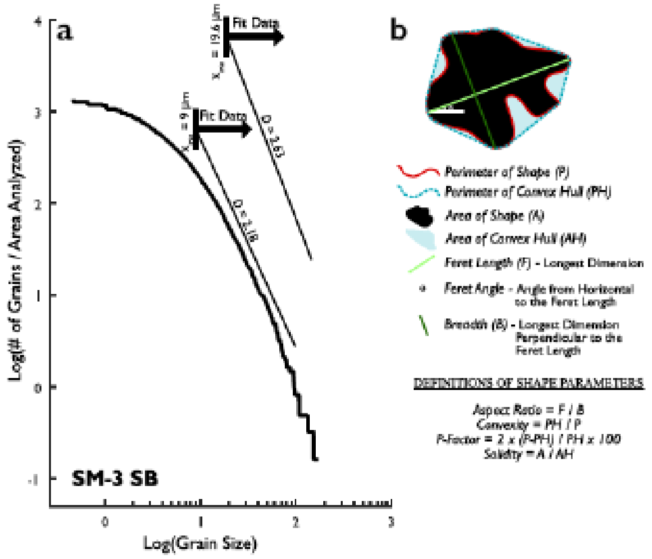

Figure 5. (a) Methods used for determining grain size distributions, using either a lower cutoff that provides the best fit to the data (in this case x_{min} = 19.6 µm), or using a consistent lower cutoff of 9 µm. All fits are reported in Table 1. (b) Definitions of the shape parameters used in this study for a given shape (black object).

$$\frac{d\theta}{dt} = -\frac{V\theta}{D_c}\ln\left(\frac{V\theta}{D_c}\right). \tag{5}$$

Fits for both aging and slip laws were obtained and are reported in Table S1; however, on plots in this paper only the aging law fits are shown to facilitate comparisons with previous experimental literature on subduction zone materials (e.g., den Hartog, Niemeijer, & Spiers, 2012; den Hartog, Peach, et al., 2012; Saffer & Marone, 2003; Zhang et al., 2017).

Sample stiffness is an important parameter which controls whether velocity-weakening materials stably slide or exhibit stick-slip behavior (Leeman et al., 2016; Scuderi et al., 2017). Sample stiffness has been shown to evolve by > 50% during experiments due to compaction, comminution, and shear localization (Leeman et al., 2016; Skarbek & Savage, 2019). Following the suggestions of Skarbek and Savage (2019), we treat sample stiffness as a fitting parameter, and find that sample stiffness ranges from 5×10^{-4} to 5×10^{-3} μm^{-1} ($\Delta\mu/\Delta x$) in our experiments (Table S1).

The saw cut geometry leads to changes in normal stress on the order of ~1.5 MPa during velocity steps (Hong & Marone, 2005; Linker & Dieterich, 1992; Perfettini et al., 2001). These changes in normal stress affect the evolution of friction (the state variable), and can be corrected using the equation derived by Linker and Dieterich (1992), where

$$\frac{d\theta}{dt} = -\alpha\frac{\theta\, d\sigma}{b\sigma\, dt} \tag{6}$$

and α is a new variable defined by

$$\alpha = \frac{\frac{\tau}{\sigma}}{\ln\left(\frac{\sigma}{\sigma_0}\right)}. \tag{7}$$

The right side of equation (6) can be added to the right side of equation (4) or (5) to correct the state variable for the effects of changing normal stress during a velocity test (Hong & Marone, 2005). The value of α can be determined through normal stress stepping experiments in a biaxial shear apparatus (Hong & Marone, 2005; Linker & Dieterich, 1992), and theoretically may vary from 0 (unaffected by normal stress perturbations) to μ_0 (maximum effect of normal stress perturbations; Perfettini et al., 2001). In geologic materials α ranges from ~1/3 to ~1/2 of steady state friction (Hong & Marone, 2005). We use a value of 0.2 for α, consistent with results for quartz-phyllosilicate mixtures in biaxial experiments (Hong & Marone, 2005), and which is ~1/3 to 1/2 of our measured friction coefficients.

2.5. Microstructures and Grain Size/Shape Analysis

Following shear experiments, the samples were air dried at room temperature, vacuum impregnated with epoxy, cut parallel to the slip direction and perpendicular to the shear plane, and dry-polished to produce a polished puck. A thin carbon coat was applied to the polished surface for scanning electron microscopy. The SEM was operated in low-vacuum mode to minimize charging effects on the gouges.

Polished thin sections were prepared from the other half of the cut sample for optical microscopy. Using a motorized stage on a petrographic microscope, stitched mosaic photographs of the experimental and natural fault rock samples were produced at 100x magnification using reflected light for clast size and shape analysis, where clasts include individual grains and polymineralic aggregates (Figures 5 and 6). After correcting for shading and stitching, high-resolution (2.2 pixels/µm) images were exported for image analysis in ImageJ.

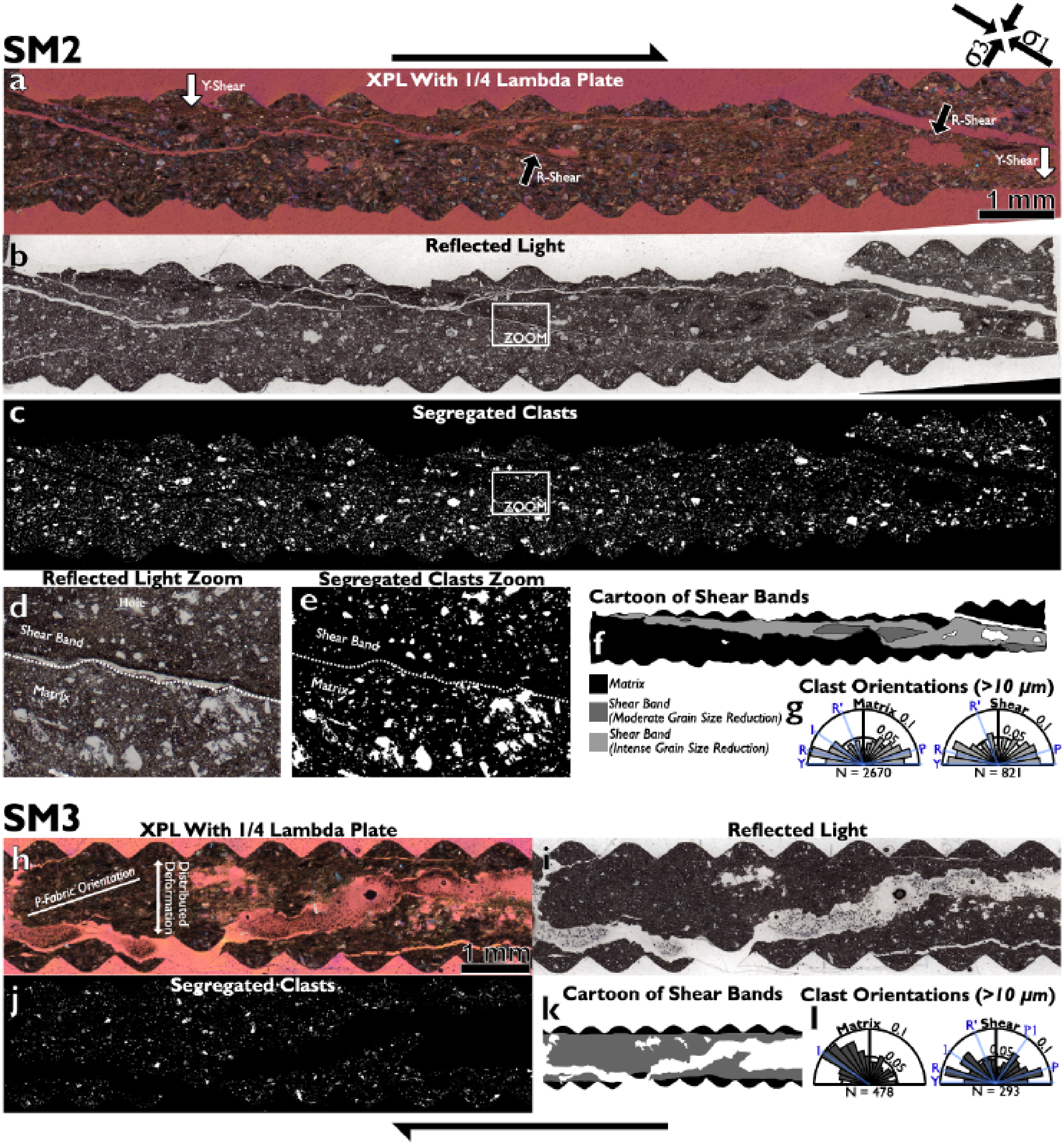

Figure 6. Photomosaics of the experimentally sheared shale samples in (a and h) cross-polarized light with a ¼ lambda plate and (b and i) reflected light. (c and j) Segregated clasts from the reflected light image used for grain shape and size analysis. Zoom of (d) the reflected light image and (e) the segregated clasts. Note the decrease in clast size within the shear band domain. (f and k) Cartoons of the microstructural domains. (g and l) Clast orientations (Feret angle) of the matrix (black from cartoons) and shear bands (greys from cartoons) for experiments on shale matrix. Clast orientations are plotted as probability density functions where bar height is equal to number of observations divided by total number of observations times the width of the bin. Bin width is 10°. Average Riedel shear orientations from Logan et al. (1992) are labeled (R, P, Y, and R′), as well as the orientation of the principal stress (1) and the orientation perpendicular to it (P1) where appropriate.

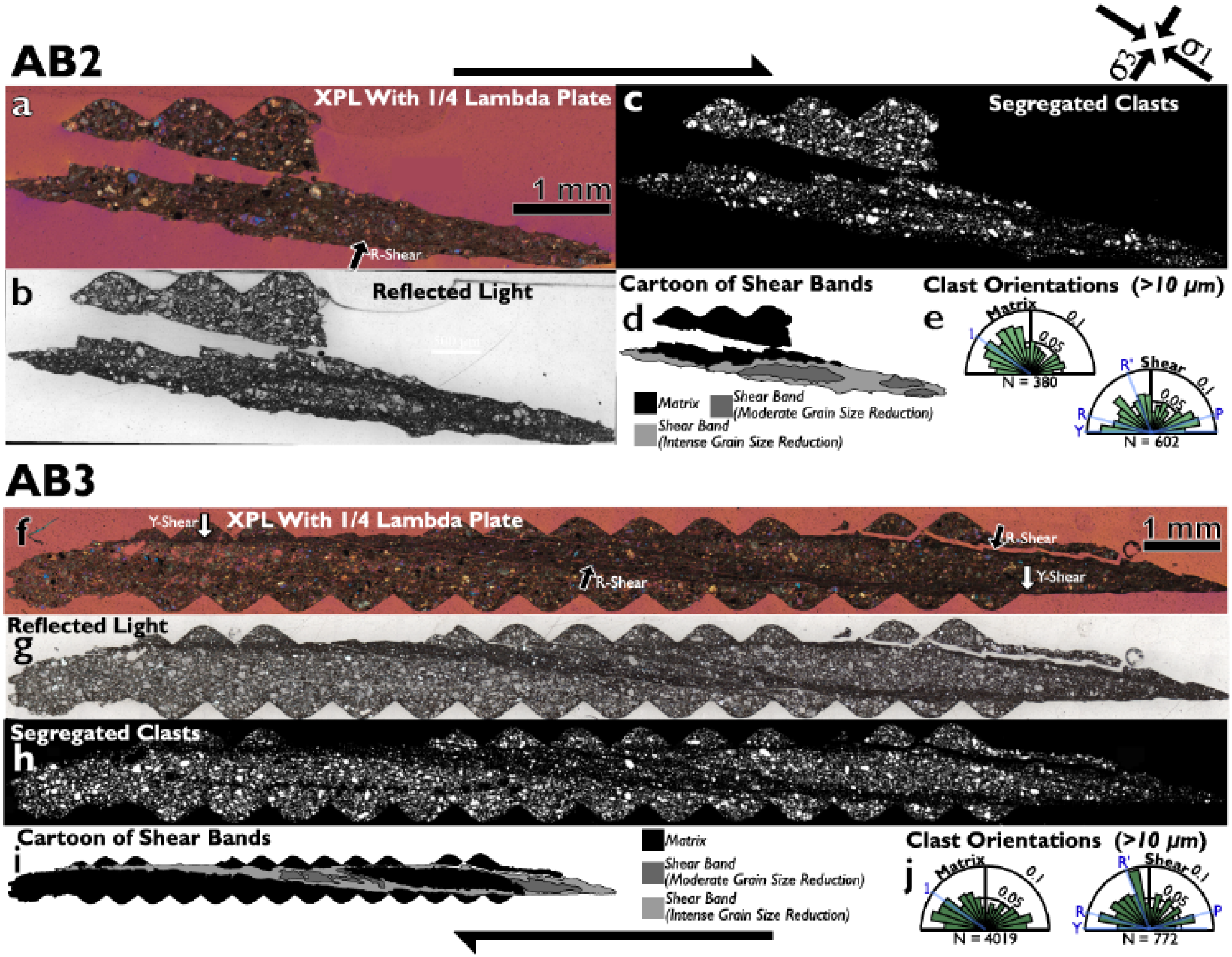

Figure 7. Photomosaics of experimentally sheared altered basalt in (a and f) cross-polarized and (b and g) reflected light. Note that AB2 had poor recovery relative to other experiments. (c and h) Segregated clasts from the reflected light image used for clast shape and size analysis. (d and i) Cartoons of the microstructural domains. (e and j) Clast orientations of the matrix (black) and shear bands (greys) for experiments on altered basalt. Clast orientations (Feret angle) are plotted as probability density functions where bar height is equal to number of observations divided by total number of observations times the width of the bin. Bin width is 10°. Average Riedel shear orientations from Logan et al. (1992) are labeled (R, P, Y, and R′), as well as the orientation of the principal stress (1) where appropriate.

To segregate clasts, we applied grey-level segmentation (five levels using the jazy Look-Up-Table macro; Heilbronner & Keulen, 2006) to each image based on their histograms. Consistent segmentation (i.e., similar bins for each image's histogram) was applied to each image. After visually comparing the segmented images with the originals to verify accurate clast segmentation, we created binary images of clasts by applying a threshold to the greyscale images, and then filled holes in individual clasts (ImageJ "fill holes" command). Cracks and physical holes were manually removed using the fill tool in ImageJ. Examples of preprocessed and postprocessed images are provided in Figures 6f and 6g. The Particles8 tool (part of the morphology toolbox) in ImageJ was used to analyze clast shapes and orientation (Landini, 2008). Analysis of both whole thin sections of recovered experimental run products and isolated areas of interest (Riedel shears and the matrix between Riedel shears) was performed to compare changes in clast sizes and shapes during deformation. Clast shape analysis was performed on all clasts with an equivalent diameter ($2\times\sqrt{area/\pi}$) greater than 10 μm, and for clasts between 3 and 10 μm (Table 3). Feret angle, solidity, convexity, Paris factor (*P*-factor),

Table 2

Calculated Fractal Dimensions (D) of the Grain Size Distributions From the Present Study for the Statistically Best Lower Cutoff (x_{min}) and for a Constant Lower Cutoff of 9 μm (See Figure 5a)

	Experimental samples												Natural samples		
	AB2-W	*AB2-M*	*AB2-SB*	*AB3-W*	*AB3-M*	*AB3-SB*	*SM2-W*	*SM2-M*	*SM2-SB*	*SM3-W*	*SM3-M*	*SM3-SB*	*AB-F*	*AB-B*	*SM*
Area of grains (%)	17.6	25.5	13.3	20.1	25.7	9.1	10	11	6.8	4.1	5.7	3.8	15.7	25.6	19.2
Area analyzed (mm^2)	4.01	0.97	2.65	14.51	9.29	4.15	21.09	13.25	6.57	9.99	2.71	6.2	2.23	36.6	11.4
Number of grains > 10 μm	1145	380	602	5024	4019	772	3753	2670	821	800	478	293	799	10325	3026
Number of grains 3–10 μm	4323	1183	2530	16579	12405	3790	16806	12182	4041	3828	2304	1411	4218	41523	18745
D values (Clauset)	1.73	1.86	1.88	1.5	1.46	1.88	2.14	1.95	2.3	2.03	1.91	2.87	3.16	1.55	2.13
x_{min}	7.9	12.79	8.69	5.23	5.23	5.98	13.24	8.07	9.7	7.19	6.6	19.63	13.15	6	7.67
p	0	0.07	0.08	0	0	0	0	0	0.45	0	0	0.6	0.31	0	0.02
D values with fixed x_{min}	1.76	1.62	1.89	1.71	1.67	2.07	1.95	1.98	2.07	2.13	2.03	2.18	2.43	1.62	2.16
x_{min}	9	9	9	9	9	9	9	9	9	9	9	9	9	9	9

Note. The *p* values are the results from the goodness-of-fit test. The *p* values above 0.1 indicate that a power law distribution is a probable fit to the grain size distributions. Note that only the shear band domains from the shale matrix and the natural altered basalt indicate that the data are well fit by a power law. M = matrix, SB = shear band, SM = shale matrix, AB = altered basalt, AB-H = natural altered basalt host, AB-F = natural fault in altered basalt.

Table 3
Mean and Median Values for Shape Factors

	Convexity		Solidity		Aspect ratio		*P*-Factor	
>10 μm	Mean	Median	Mean	Median	Mean	Median	Mean	Median
SM	0.66	0.66	0.64	0.63	1.66	1.52	128	101
SM2-M	0.80	0.82	0.77	0.80	1.72	1.58	58	42
SM2-SB	0.82	0.86	0.80	0.83	1.74	1.54	50	33
SM3-M	0.79	0.81	0.74	0.76	1.82	1.66	62	46
SM3-SB	0.80	0.83	0.76	0.79	1.73	1.56	58	40
AB-H	0.71	0.72	0.68	0.68	1.63	1.53	100	77
AB-F	0.73	0.74	0.68	0.69	1.59	1.49	86	70
AB2-M	0.76	0.78	0.78	0.78	1.62	1.52	73	56
AB2-SB	0.77	0.80	0.79	0.82	1.58	1.50	68	51
AB3-M	0.77	0.79	0.77	0.79	1.62	1.51	70	53
AB3-SB	0.80	0.83	0.81	0.83	1.52	1.43	57	42
3–10 μm								
SM	0.86	0.88	0.73	0.75	1.68	1.57	35	26
SM2-M	0.92	0.94	0.83	0.88	1.80	1.64	18	12
SM2-SB	0.93	0.95	0.86	0.90	1.76	1.58	16	10
SM3-M	0.92	0.95	0.83	0.87	1.91	1.72	18	12
SM3-SB	0.93	0.95	0.83	0.87	1.88	1.69	17	11
AB-H	0.88	0.90	0.75	0.78	1.69	1.58	31	22
AB-F	0.87	0.90	0.75	0.77	1.68	1.56	32	23
AB2-M	0.91	0.94	0.83	0.86	1.71	1.58	21	14
AB2-SB	0.91	0.94	0.83	0.87	1.63	1.50	21	13
AB3-M	0.92	0.94	0.84	0.88	1.66	1.54	19	12
AB3-SB	0.92	0.95	0.85	0.89	1.60	1.48	18	11

Note. M = matrix, SB = shear band, SM = shale matrix, AB = altered basalt, AB-H = natural altered basalt host, AB-F = natural fault in altered basalt.

and aspect ratio were analyzed for whole thin sections and isolated areas of interest (for definitions of shape factors see Figure 5b; Heilbronner & Keulen, 2006). Clast orientations were plotted as particle density functions (Figures 2b, 6g, 6l, 7e, and 7j).

Grain size distributions were measured on thin sections cut from each experimentally deformed sample and for the natural mélange samples (Figure 2a). We followed the technique of Blenkinsop (1991), where grains are not binned, and the logarithm of total number of grains below a given grain size (divided by area analyzed) is plotted (Figure 5a). This technique was used over the other common method where grains are binned (Keulen et al., 2007; Marone & Scholz, 1989; Sammis et al., 1986), since binning data have been shown to decrease the accuracy of fits to power law data and to underestimate the value of *D* (Virkar & Clauset, 2014). Fractal dimensions (*D*; the slope of a linear fit to the grain size distributions) were calculated for each grain size distribution. Fits were performed following the methods outlined in Clauset et al. (2009) for fitting power laws to empirical data, which uses maximum likelihood rather than least squares regression for establishing the scaling exponent. For each grain size distribution we determined a lower bound to the fit (x_{min}) using the Kolmogorov-Smirnov goodness-of-fit statistic, outlined in detail in Clauset et al. (2009). However, because of the wide range in values of x_{min} determined for each grain size distribution, we performed a second fit with a constant x_{min} of 9 μm (the average x_{min} of the samples as determined by the Kolmogorov-Smirnov goodness-of-fit statistic) to facilitate direct comparison of values determined in this study. The *D* values determined through these methods are larger than those determined through least squares regression. We calculated fits using least squares regression to see the effect (Figure S4 and Table S2), and found that the fractal dimensions are ~0.3 to 0.5 higher for the fits determined using maximum likelihood. Finally, a goodness of fit test (*p* value, where synthetic data sets with identical *D* and x_{min} are compared with the natural data) was used to determine the likelihood that the grain size distributions indeed follow a power law distribution (Table 2; Clauset et al., 2009). We note that most of the samples here show a poor likelihood of being best described by a power law; however, we use the power law framework to facilitate comparison with previous studies on grain size distributions.

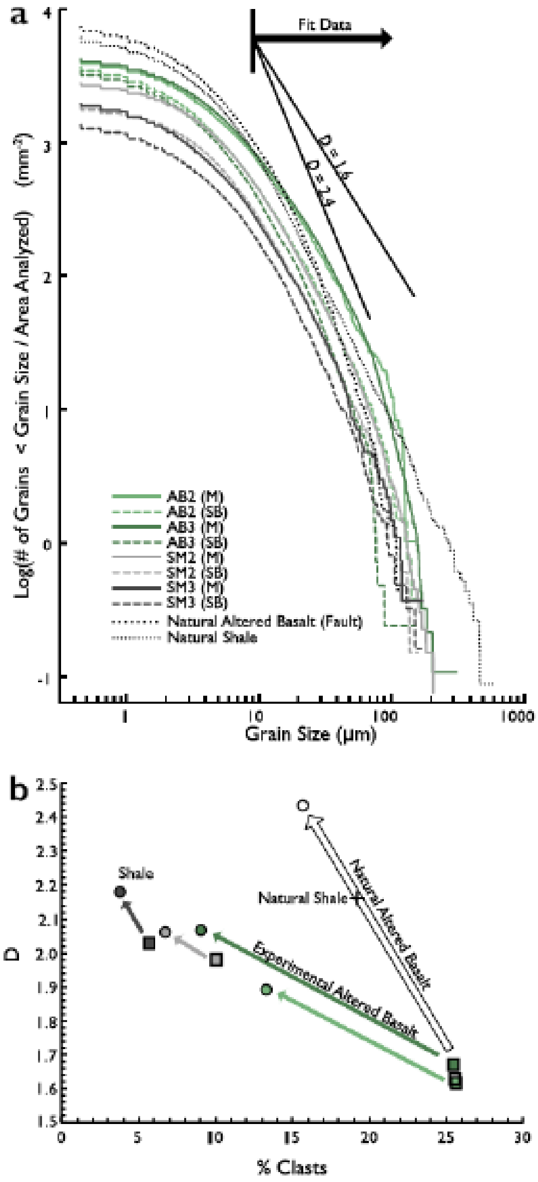

Figure 8. (a) Grain size distributions for the experimental run products and the natural microstructures using the approach of Blenkinsop (1991). The fit interval (>9 μm) is used in the calculation of the fractal dimension, *D*. Solid black lines show the range of slopes for the calculated values of *D*. (b) Evolution of the grain size distribution from the matrix (squares) to shear bands (circles) for each of the experiments (using a consistent x_{min} of 9 μm). For the natural altered basalt, the evolution from the host to the fault is shown.

3. Results

3.1. X-ray Diffraction

Analysis of random powders shows that the altered basalt is predominantly composed of albite and chamosite (chlorite), while the shale is composed of quartz, illite, and albite (Figure 3). The modal proportion of phyllosilicates is ~25 and ~40 % for the altered basalt and shale samples, respectively (Figures 3a and 3b). In the oriented clay separates, neither unit shows evidence for expanding clays (i.e., smectites; Figures 3c and 3d).

3.2. Rate-and-State Friction Parameters

Shale was frictionally weaker ($\mu = 0.48$–0.51) than the altered basalt ($\mu = 0.60$–0.69) for velocities of 0.2 and 2 μm/s in all experiments (Figure 4b and Table S1). All experiments show strain-hardening behavior, and the magnitude of hardening is greater at a pore fluid factor of 0.36 than at 0.7 (Figure 4b). Altering the pore fluid factor had little effect on the coefficient of friction at yield, although the lower degree of strain hardening throughout the experiment led to a coefficient of friction that is ~0.02 to 0.06 lower by the end of experiments with elevated fluid pressures.

The shale exhibits velocity-strengthening behavior with a negligible evolution effect (*b*), while the altered basalt exhibits velocity-weakening behavior (Figures 4c and 4d and Table S1). At the fastest rate step (2.0 to 20 μm/s) both lithologies exhibit linear strain-hardening and apparent velocity-strengthening behavior, which may reflect disequilibrium of pore fluid pressure at the highest velocity (20 μm/s). For altered basalt, D_c is lower at a pore fluid factor of 0.7 relative to 0.36 (Figures 4c–4e). This change is not observable in the shale due to the negligible evolution effect (Figures 4c and 4d).

3.3. Microstructures of Experimentally Deformed Samples

Deformation of the experimental samples was predominantly accommodated in localized Riedel shears. The shears are a few hundred microns wide (variable) and locally anastomose, but generally occur in a Y-orientation (parallel with the imposed slip direction; Logan et al., 1979, 1992). Riedel shears can be identified by a greatly reduced grain size and a dark appearance in both cross-polarized and reflected light (Figures 6a, 6b, 6h, 6i, 7a, 7b, 7f, and 7g). The Y-shears occur near the contact with the forcing blocks (Figures 6a and 7f), as is commonly observed in triaxial friction experiments (Haines et al., 2013; Logan et al., 1979, 1992; Marone et al., 1990; Tembe et al., 2010). R-shears developed during several experiments and are visible in thin sections of samples with the best recovery (SM2 and AB3). R-shears allowed displacement along the principal Y-shear to be transferred from the margin of one forcing block to the forcing block on the other side (Figures 6a and 7f; Marone, 1998). In shale deformed during experiment SM2, Riedel shears contain strongly aligned phyllosilicates, as seen by the uniform color in cross polarized light photomicrographs with the lambda plate inserted (Figures 6a and 6h). In contrast, Riedel shears in the altered basalt samples show a poor alignment of phyllosilicates (Figure 7). The shale experiment at high pore fluid pressure (SM3) is an exception to the above description, and does not show localized shear surfaces in Y- and R-orientations. Instead, it displays a well-developed P-fabric indicating distributed deformation across the width of the sample (Figure 6h).

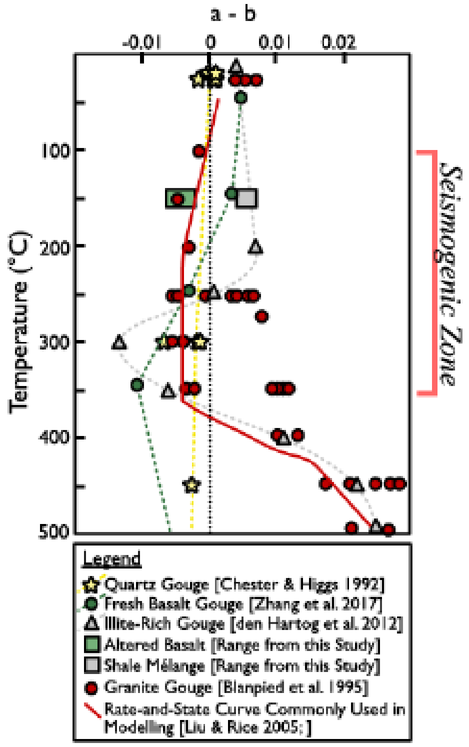

Figure 9. Velocity dependence of friction with temperature used in models and for some common subduction zone lithologies. Many modeling studies use the results of Blanpied et al. (1995; solid red line), derived from experiments on granite (red circles), while results from more realistic subduction zone materials (illite gouge and basalt) tend to shift velocity-weakening behavior to greater depths than the observed seismogenic zone (demarcation of thermally defined seismogenic zone based on Hyndman et al. (1997)). Note that illite-rich gouge, shale mélange from this study, and basalt all show velocity-strengthening behavior at the updip limit of the seismogenic zone, while the altered basalt from this study exhibits velocity-weakening behavior.

The orientation of clasts (>10 μm) changes between the matrix and shear band domains (Figures 6g, 6l, 7e, and 7j). In the matrix of altered basalt samples, the long axes of clasts are aligned parallel to the maximum principal stress, σ_1 (i.e., ~30° to the shear plane). Backscattered electron SEM images of the experimentally sheared samples show that tensile fractures in large clasts from the altered basalt are also predominantly oriented parallel to σ_1 (~30° to the shear plane; Figures S1 and S2). In the shale samples, fracturing of large clasts occurs parallel to the preexisting foliation within clasts (Figures S1 and S2), which results in tensile fractures oriented ~60° from the shear direction (30° to σ_1) in these samples. In both the shale and altered basalt, the majority of tensile fractures are observed in large clasts within the matrix between Riedel shears (Figures S1 and S2). In the shear band domains of all samples, clasts show a strong alignment in R- and P-orientations, and moderate to strong alignment in the Y-orientation (Figures 6g, 6l, 7e, and 7j). In the shale sample showing distributed deformation (SM3), there is an alignment of clasts perpendicular to σ_1 and parallel to the minimum principal stress, σ_3 (Figure 6l).

Clast shape factors vary systematically between the matrix and shear band domains, with higher convexity and solidity, and lower aspect ratio and *P*-factor in shear band domains (Table 3). Clasts larger than 10 μm experienced a greater percent change in each shape factor than clasts between 3 and 10 μm (Table 3). As in previous studies, grain size distributions showed an increase in the value of *D* between matrix and shear bands, and a direct correlation between *D* value and percent clasts (Figure 8b and Table 2; Marone & Scholz, 1989; Heilbronner & Keulen, 2006; Keulen et al., 2007). Altered basalt showed a progression from *D* values of ~1.6 in the matrix to *D* values of 1.9–2.1 in the shear bands, while shale *D* values (from both matrix and shear bands) fell between 1.9 and 2.1 (Figure 8b). The results from the altered basalt are comparable to previous experiments showing the evolution of fractal dimension with shear strain. In the high-strain ($\gamma > 1.5$) experiments of Marone and Scholz (1989) on quartz gouges, the fractal dimension was ~1.6 in the bulk sample, while shear bands had higher fractal dimensions ranging from ~2 to 2.8.

3.4. Microstructures of Natural Samples

Clast sizes and shapes were analyzed for the natural shale matrix, the altered basalt, and a fault cutting through the altered basalt (Figure 2). The clast size distribution from the natural shale matrix shows a moderate *D* value (~2.1; Figure 8b). Clasts in the shale matrix exhibit a strong shape preferred orientation parallel with the principal foliation observed in thin section (Figure 2b). The natural shale displays the lowest solidity and convexity values of any sample, the lowest clast aspect ratio of any shale sample, and a higher *P*-factor than any experimentally sheared shale sample (Table 3).

Clasts from the altered basalt show no shape-preferred orientation, while clasts from the fault cutting through the altered basalt show shape-preferred orientations in R- and P-Riedel orientations (Figure 2b). Convexity and solidity values are lower than for clasts in the experimentally deformed altered basalt, and there is a slight increase in these values from the host altered basalt to the fault cutting through the altered basalt (Table 3). The naturally faulted samples show a larger proportion of smaller clasts per unit area (<10 μm) than the experimental samples (Figure 8a). The *D* value for the altered basalt host is comparable to the matrix between shear bands in the experimental samples (Figure 8b). However, the natural fault cutting through the altered basalt shows a higher fractal dimension (*D*) than either the matrix or shear bands of the experimental faults, while maintaining a higher percentage of clasts than the experimental shear bands (Figure 8b).

4. Interpretations

4.1. Interpretation of Experimental Results and Microstructures

The difference in coefficient of friction between the altered basalt and shale may be explained by the relative phyllosilicate abundances of the two samples. The shale contains a larger proportion of phyllosilicates (~40%) compared with the altered basalt (~25%). The relationship between phyllosilicate content and coefficient of friction at low temperatures is complex. Some studies show a sudden weakening in the coefficient of friction once a threshold in the phyllosilicate content is reached (Escartin et al., 2001; Giorgetti et al., 2015), while others show a linear relationship between phyllosilicate content and strength (Tembe et al., 2010, and references within). The type of response may depend on the species of phyllosilicate (e.g., illite and chlorite for linear trend versus serpentine and talc for sudden weakening). Given that the coefficient of friction for both albite and quartz (the dominant framework silicate in each sample) is about ~0.7 (Chester & Higgs, 1992; He et al., 2013), and that the coefficient of friction for wet illite and chlorite at low temperatures is ~0.3 (Behnsen & Faulkner, 2012), the obtained coefficients of friction (μ = ~0.65 for altered basalt and ~0.5 for shale) are in agreement with the predictions of Tembe et al. (2010) for a linear relationship between sample strength and phyllosilicate content (Figure 4; their Figure 4b).

The rate-and-state properties of the shale matrix are comparable to previous experiments on illite-rich shales at low to moderate temperatures (den Hartog, Peach, et al., 2012; Ikari et al., 2009; Saffer & Marone, 2003), which all show velocity-strengthening behavior at temperatures below 250 °C (Figure 9). The velocity-weakening behavior of altered basalt, however, is in contrast to the frictional behavior of fresh basalt (Zhang et al., 2017) and fresh gabbro (He et al., 2007), which are both velocity-strengthening at temperatures below 250 °C (Figure 9). The alteration of basalt at Mugi led to an increase in albite at the expense of pyroxene (~10% change in each; Figure S5). Pyroxene is approximately velocity neutral while albite is velocity weakening (He et al., 2013). The replacement of pyroxene by plagioclase may therefore push altered basalt into the velocity-weakening regime (He et al., 2013).

At the fastest slip rate (20 μm/s), both lithologies exhibited linear strain hardening, and apparent velocity-strengthening behavior. An increase in the hardening rate with increasing slip rate is frequently observed in triaxial friction experiments (den Hartog, Peach, et al., 2012; Tembe et al., 2010); however, the physical mechanism for this relationship remains poorly understood. One possible reason for the linear strain hardening is fluid overpressure due to undrained conditions; however, the initial response (rapid strengthening) is opposite to that predicted for fluid overpressure (initial weakening followed by strengthening; Faulkner et al., 2017). In our experiments, the rate of strain hardening greatly increased during the fastest rate steps, and the coefficient of friction did not achieve a new steady state, preventing the determination of rate-and-state friction parameters. If the hardening during the fastest rate step represents a phenomenon that occurs in nature, then it may provide a mechanism for self-arrest with increasing velocity (a potential mechanism for slow slip; e.g., Hawthorne & Rubin, 2013; Ikari et al., 2013). This has been previously hypothesized by Ikari et al. (2013) for the generation of slow earthquakes. In a series of experiments on shale, strain-weakening was observed at low displacement rates (~0.2 to 8 μm/s) in samples from a décollement, which then strain hardened at faster displacement rates. Following Ikari et al. (2013), we fit the last 300 μm of each rate step to determine the slip dependence on friction ($d\mu/dx$). Our strengthening trend in the fastest rate steps (20 μm/s) is higher (0.046 and 0.063 mm^{-1} for the altered basalt and shale, respectively) than those recorded by Ikari et al. (2013) (always <~0.007 mm^{-1}). At low velocities (0.20 and 2.0 μm/s) the strengthening trend ranges from 0.0067 to 0.033 mm^{-1} (Table S1).

The microstructures from our experimentally sheared samples may provide insights into the processes that control the rate-and-state strength of the two rock types that are representative of the Mugi Mélange. A major difference between the altered basalt and the shale matrix is in the evolution of friction following a rate-step (b), which has long been thought to reflect the evolution of asperity contact areas and strengths (through chemical and physical time-dependent processes) following a rate-step (Rabinowicz, 1951, 1958). The lack of an evolution in friction coefficient following a rate-step (i.e., negligible to negative b value) in the shale may be due to the aligned phyllosilicates observed in the photomicrographs of the deformed shale (Figures 6a and 6h). Slip parallel to aligned phyllosilicates would not change contact area during slip following a rate-step, and would therefore not show an evolution of friction during subsequent slip (Ikari et al., 2013). This has been observed previously in biaxial experiments on phyllosilicate-rich rocks, including illite schists, chloritic schists, and montmorillonite-quartz mixtures (Ikari et al., 2009) as well as smectite-rich samples (Carpenter et al., 2015; Saffer & Marone, 2003), and our results show the same behavior at 150 °C as documented in these earlier room-temperature experiments (Figures 4b–4d).

Increasing the pore fluid factor was found to decrease the critical slip distance (D_c) for experiments on altered basalts, as has been previously observed in calcareous gouges (Figure 4f; Scuderi & Collettini, 2016). This is interpreted to be due to the decreased effective normal stress on the system, which would reduce contact area at the grain junctions for the altered basalt, and allow for faster equilibration of grain contacts following a rate-step (Scuderi & Collettini, 2016).

We note that the strengths and velocity dependence of the materials determined in this study may change at plate-rate velocities, where low-temperature crystal plasticity of the phyllosilicates (French et al., 2015) and/or pressure solution in quartz (den Hartog & Spiers, 2014; Fagereng & den Hartog, 2016; Phillips & White, 2017) may become important mechanisms that affect the frictional properties. However, the experimental conditions are likely similar to those in subduction plate boundaries, and at these slip rates are expected to be applicable to the slip rates during earthquake nucleation and for slow slip.

4.2. Comparison of the Natural and Experimental Microstructures

The shape factors of the natural shale samples from the mélange matrix differentiate it from the experimental samples which were ground to <125-μm grain size prior to shearing (Table 3). Despite a lower aspect ratio than the experimental samples, the shape factors for the natural shale are less rounded than the experimental samples, and a strong shape-preferred orientation parallel with the foliation is observed in plane-polarized light. This contrasts with the shear bands formed during the experiments, which show a greater roundness of clasts with lower aspect ratios, and a shape-preferred orientation of clasts parallel to R- and P-Riedel shears. This difference reflects the dominance of solution processes in developing the natural shale fabrics, which cannot effectively create fabric on short laboratory time scales. Previous geochemical studies of the Mugi mélange support the importance of solution in the shale matrix (Kawabata et al., 2007, 2009).

In the natural altered basalt, we see a progression in grain size distributions and shape factors from the host to the fault that are similar to the changes from the matrix to the shear bands in experiments. The fractal dimension of the grain size distribution increases and there is a change in shape factors indicating greater roundness of clasts (Tables 2 and 3). Clast orientations show a shape-preferred orientation parallel to Riedel shears (Figure 2b). These observations indicate that the faults in the altered basalt formed through cataclasis and frictional sliding. One notable difference between the fault in the natural altered basalt and the experimental shear bands is in the proportion of clasts. The natural fault has a higher proportion of clasts compared to the shear bands in experiments. This may be due to postfracturing grain growth (Sammis & Ben-Zion, 2008), precipitation of minerals from fluids in the fault following slip (e.g., fault healing; Williams et al., 2015), and/or agglomeration of grains.

The natural microstructures indicate that distributed deformation in the shale was accommodated through pressure solution-accommodated creep, while the altered basalt deformed through localized cataclasis and frictional sliding. In the experiments, both rock types deformed through cataclasis and frictional sliding.

5. Discussion

5.1. Implications for the Seismogenic Zone

The depth distribution of earthquake hypocenters has been used to define a seismogenic zone, where the majority of earthquakes nucleate, for faults from various tectonic settings (e.g., Hyndman et al., 1997; Marone & Scholz, 1988; Oleskevich et al., 1999; Sibson, 1982). The updip limit of the seismogenic zone is hypothesized to be controlled by the rate-and-state frictional properties of fault rocks (Marone & Scholz, 1988; Scholz, 1998). Within subduction zones, the seismogenic zone correlates well with temperature, with the updip limit beginning between 100 and 150 °C (Hyndman et al., 1997). The change in frictional properties with increasing temperature is thought to be controlled by diagenetic-metamorphic processes in subduction zones, and the updip limit approximately correlates with the smectite to illite clay transition, declining fluid production (and an associated decrease in pore fluid pressures), and an increase in pressure solution and quartz cementation rates (Moore et al., 2007; Moore & Saffer, 2001).

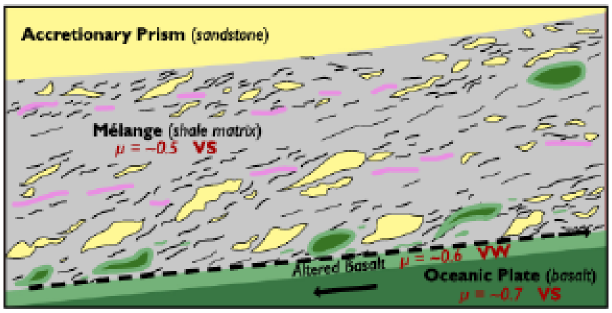

Figure 10. Cartoon of the shallow subduction interface based on the geology of the Mugi Mélange (before thrust imbrication). The shale matrix, which exhibits velocity-strengthening (VS) behavior, is unlikely to nucleate earthquakes, while the altered basalt which exhibits velocity-weakening (VW) behavior may promote localized deformation. Once nucleated, earthquakes may preferentially propagate along the interface between the mélange and altered basalt (Phillips et al., 2019; Ujiie, Yamaguchi, Kimura, & Toh, 2007). Basaltic blocks with altered margins embedded within the shale matrix may be nucleation sites for (very) low frequency earthquakes at high pore fluid pressures, or repeating microseismic events at low pore fluid pressures. Thin black lines exhibit the foliation, while pink lines are discontinuous tuffs.

A challenge with using the rate-and-state framework to explain the updip limit of the seismogenic zone is that most rock types found in subduction thrust faults (e.g., shale (den Hartog, Niemeijer, & Spiers, 2012; Ikari et al., 2009; Saffer & Marone, 2003), calcareous sediments (Rabinowitz et al., 2018), gabbro (He et al., 2007), and basalt (Zhang et al., 2017)) show velocity-strengthening behavior around the updip limit of the seismogenic zone, inconsistent with the observed distribution of seismicity (Figure 9; Obana et al., 2001). Additionally, illite exhibits velocity-strengthening behavior near the updip limit of the seismogenic zone (Saffer & Marone, 2003). Since earthquake nucleation is expected to occur in materials with velocity-weakening behavior (Scholz, 1998), we should investigate the possibility that other lithologies present at the subduction interface may exhibit velocity-weakening behavior. Evidence of seismic slip has been found along the margins of altered basalts from both the upper and lower units in the Mugi Mélange (Phillips et al., 2019; Ujiie, Yamaguchi, Kimura, & Toh, 2007), and our experiments have shown that this rock type exhibits velocity-weakening behavior at 150 °C. In contrast, the shale exhibits velocity-strengthening behavior at 150 °C, and microstructures of natural shale from Mugi indicates that it deformed through pressure solution accommodated creep. We hypothesize that altered basalt, a ubiquitous subduction zone material, may be responsible for seismicity at the updip limit of the seismogenic zone. Experiments on fresh, unaltered basalt, or even hydrothermally altered basalt, may not be applicable to the conditions of the subduction zone interface because of differences in their mineralogy (e.g., Humphris & Thompson, 1977; Seyfried & Bischoff, 1979). Therefore, further experimental studies on altered basalt are required to fully characterize its behavior through a range of subduction zone conditions.

5.2. Implications for Shallow Slow Earthquake Phenomena

Mixing velocity-weakening and strengthening materials is one proposed mechanism for tremor containing low and very low frequency earthquakes (Ando et al., 2010; Hayman & Lavier, 2014; Skarbek et al., 2012). Within these models, failure of blocks of velocity-weakening materials embedded within a velocity-strengthening matrix leads to very low frequency earthquakes or low frequency earthquakes, which together make a tremor-like signal. At the downdip limit of the seismogenic zone, these are often envisaged as strong, competent, blocks sitting within a ductile matrix deforming through crystal plastic creep (Hayman & Lavier, 2014; Kotowski & Behr, 2019) or pressure solution creep (Fagereng & den Hartog, 2016). At the updip limit of the seismogenic zone the matrix accommodates distributed deformation through pressure solution creep and/or distributed frictional sliding (Moore & Saffer, 2001). In either case, a fracture propagating from a velocity-weakening block (of appropriate size, see below) should be quickly arrested by the velocity-strengthening behavior of the shale, which could lead to a low frequency or very low frequency event. Basaltic blocks, with velocity-weakening altered margins, could serve as nucleation points for very low frequency and low frequency earthquakes if they are embedded within a velocity-strengthening matrix (Figure 10). (Very) low frequency earthquakes frequently occur in sequences (e.g., Wech & Bartlow, 2014). Sequences of low frequency earthquakes could occur by progressive failure of velocity-weakening blocks due to progressive transfer of stresses or when blocks are separated by a critical spacing. Given that shale matrix transitions to velocity-weakening behavior at temperatures above ~250 °C (Ujiie, Yamaguchi, Kimura, & Toh, 2007), this limits the zone of mixed velocity-weakening and strengthening materials to shallow depths along the subduction interface, consistent with the observation that shallow slow earthquakes and associated tremor occur below ~230 °C (Saffer & Wallace, 2015). It is important to note that the temperature of the transition (from velocity-strengthening to weakening) would change depending on the composition of the matrix. For example, at the Hikurangi margin, where fossiliferous, calcareous oozes mixed with silty clays form the dominant subducting sediments above the oceanic plate, the carbonate dominated matrix may exhibit velocity-strengthening behavior to greater depths than an illite-rich shale matrix (Rabinowitz et al., 2018). In addition, high pore fluid factors are likely required for low frequency earthquakes and slow slip. These are observed in regions of tremor and slow slip in shallow subduction zones

(Tonegawa et al., 2017), and are often required in models of tremor using mixed lithologies (e.g., Skarbek et al., 2012).

In the experiments presented here, elevating the pore fluid factor had two key effects: (1) it led to a decrease in the critical slip distance D_c in the altered basalt and (2) it decreased the effective normal stress (σ_n) on the sample. These changes would affect the critical nucleation length required for unstable slip (Rubin & Ampuero, 2005; Uenishi & Rice, 2003). The critical nucleation length (L) is described by

$$L = 2{*}C{*}\left(\mu'{*}\frac{D_c}{b\sigma_n}\right) \tag{8}$$

where μ' is the shear modulus and C is a numerical constant (with a value between 1 and 1.5). Note that increasing the pore fluid pressure introduces competing effects on the critical nucleation length by decreasing critical slip distance (thereby decreasing L) and also decreasing the effective normal stress (thereby increasing L). The final effect on the critical nucleation length (whether it increases or decreases) would depend on the relative changes of these two properties with increasing pore fluid pressure. If we compare results from the upsteps in velocities from experiments AB2 ($\lambda = 0.36$) and AB3 ($\lambda = 0.7$), we find that increasing the fluid pressure would increase the critical nucleation length for unstable slip by ~1.5 times. The experiments performed here indicate that the reduction in normal stress from increasing the pore fluid pressure has a greater effect on the critical nucleation length than the reduction in critical slip distance.

In models of slow slip, a critical factor controlling slip style (slow slip versus earthquake) is the ratio between the width (W) of the source zone and the critical nucleation length (i.e., W/L; Liu & Rice, 2007; Rubin, 2008), with large values promoting unstable slip and moderate values promoting aseismic transients with low frequency earthquakes. If we consider blocks of altered basalt as potential nucleation sites (of fixed width) for unstable slip, increasing the pore fluid pressure on the system would decrease the ratio (W/L), promoting aseismic transients with low-frequency earthquakes.

Our results extend to the layer of altered basalt along the upper interface of all subducting oceanic plates. The layer of altered basalt at the upper interface of subducting oceanic plates may influence seismicity in two ways. Firstly, it may provide a velocity-weakening interface for seismic events to nucleate from. Secondly, while at low temperatures of ~150 °C, the altered basalt may provide a source of velocity-weakening materials to mix with the velocity-strengthening subducting sediments, resulting in complex behavior (tremor, very low frequency earthquakes, and low-frequency earthquakes) at elevated pore fluid pressure conditions (Figure 10).

6. Conclusions

The frictional properties of subducting materials likely control the mode of slip in shallow subduction zones. Altered basalt, a ubiquitous subduction zone material, exhibits velocity-weakening behavior near the updip limit of the seismogenic zone, while the surrounding shale matrix exhibits velocity-strengthening behavior. We hypothesize that earthquakes may preferentially nucleate in altered basalt at the updip limit of the seismogenic zone, and that mixing of velocity-weakening altered basalt and velocity-strengthening sediments above the plate interface may lead to complex modes of deformation (tremor, very low frequency earthquakes, and low-frequency earthquakes).

Acknowledgments

N.J.P. was supported by a Graduate Mobility Award from McGill University, GSA student grant 11283-16, the Japan Society for the Promotion of Science KAKENHI grant JP16K21728, and an NSERC PGS-D, M. F. by NSF EAR1759127, C.R. by an NSERC Discovery Grant and Canada Research Chair in Earthquake Geology, and K.U. by the Japan Society for the Promotion of Science KAKENHI grant JP16H06476. Raw data sets for this research are available in an OSF data repository which can be accessed with the following DOI: 10.17605/OSF.IO/W2GB4. The authors thank Chris Marone and an anonymous reviewer for the constructive comments that helped to improve the manuscript. N.J. P. would like to thank the Rosses for being sublime hosts during his time at Rice University.

References

Ando, R., Nakata, R., & Hori, T. (2010). A slip pulse model with fault heterogeneity for low-frequency earthquakes and tremor along plate interfaces. *Geophysical Research Letters*, *37*, L10310. https://doi.org/10.1029/2010GL043056

Araki, E., Saffer, D. M., Kopf, A. J., Wallace, L. M., Kimura, T., Machida, Y., et al., & IODP Expedition 365 Shipboard Scientists (2017). Recurring and triggered slow-slip events near the trench at the Nankai Trough subduction megathrust. *Science*, *356*, 1157–1160.

Avouac, J. (2015). From geodetic imaging of seismic and aseismic fault slip to dynamic modeling of the seismic cycle. *Annual Review of Earth and Planetary Sciences*, *43*, 233–271. https://doi.org/10.1146/annurev-earth-060614-105302

Behnsen, J., & Faulkner, D. R. (2012). The effect of mineralogy and effective normal stress on frictional strength of sheet silicates. *Journal of Structural Geology*, *42*, 49–61. https://doi.org/10.1016/j.jsg.2012.06.015

Beroza, G. C., & Ide, S. (2011). Slow earthquakes and nonvolcanic tremor. *Annual Review of Earth and Planetary Sciences*, *39*(1), 271–296. https://doi.org/10.1146/annurev-earth-040809-152531

Bilek, S. L., & Lay, T. (1999). Rigidity variations with depth along interplate megathrust faults in subduction zones. *Nature*, *400*, 443–446. https://doi.org/10.1038/22739

Blanpied, M. L., Lockner, D. A., & Byerlee, J. D. (1995). Frictional slip of granite at hydrothermal conditions. *Journal of Geophysical Research*, *100*(B7), 13,045–13,064. https://doi.org/10.1029/95JB00862

Blenkinsop, T. G. (1991). Cataclasis and processes of particle size reduction. *Pure and Applied Geophysics*, *136*(1), 59–86. https://doi.org/10.1007/BF00878888

Bürgmann, R. (2018). The geophysics, geology and mechanics of slow fault slip. *Earth and Planetary Science Letters*, *495*, 112–134. https://doi.org/10.1016/j.epsl.2018.04.062

Carpenter, B. M., Saffer, D. M., & Marone, C. (2015). Frictional properties of the active San Andreas Fault at SAFOD: Implications for fault strength and slip behavior. *Journal of Geophysical Research: Solid Earth*, *120*, 1–17. https://doi.org/10.1002/2015JB011963.Received

Chester, F. M., & Higgs, N. G. (1992). Multimechanism friction constitutive model for ultrafine quartz gouge at hypocentral conditions. *Journal of Geophysical Research*, *97*(B2), 1859–1870.

Clauset, A., Shalizi, C. R., & Newman, M. E. J. (2009). Power-law distributions in empirical data. *SIAM Review*, *51*(4), 661–703.

Coble, C. G., French, M. E., Chester, F. M., Chester, J. S., & Kitajima, H. (2014). In situ frictional properties of San Andreas Fault gouge at SAFOD. *Geophysical Journal International*, *199*(2), 956–967. https://doi.org/10.1093/gji/ggu306

Cowan, D. S. (1985). Structural styles in Mesozoic and Cenozoic mélanges in the western Cordillera of North America. *Geological Society of America Bulletin*, *96*(4), 451–462. https://doi.org/10.1130/0016-7606(1985)96<451:SSIMAC>2.0.CO;2

den Hartog, S. A. M., Niemeijer, A. R., & Spiers, C. J. (2012). New constraints on megathrust slip stability under subduction zone P-T conditions. *Earth and Planetary Science Letters*, *353–354*, 240–252. https://doi.org/10.1016/j.epsl.2012.08.022

den Hartog, S. A. M., Peach, C. J., de Winter, D. A. M., Spiers, C. J., & Shimamoto, T. (2012). Frictional properties of megathrust fault gouges at low sliding velocities: New data on effects of normal stress and temperature. *Journal of Structural Geology*, *38*, 156–171. https://doi.org/10.1016/j.jsg.2011.12.001

den Hartog, S. A. M., & Spiers, C. J. (2014). A microphysical model for fault gouge friction applied to subduction megathrusts. *Journal of Geophysical Research: Solid Earth*, *119*, 1510–1529. https://doi.org/10.1002/2014JB011151.Received

Dieterich, J. H. (1978). Time-dependent friction and the mechanics of stick-slip. *Pure and Applied Geophysics*, *116*, 790–806.

Escartin, J., Hirth, G., & Evans, B. (2001). Strength of slightly serpentinized peridotites: Implications for the tectonics of oceanic lithosphere. *Geology*, *29*(11), 1023–1026.

Fagereng, Å. (2011). Geology of the seismogenic subduction thrust interface. *Geological Society of London, Special Publication*, *359*, 55–76. https://doi.org/10.1144/SP359.4

Fagereng, Å., & den Hartog, S. A. M. (2016). Subduction megathrust creep governed by pressure solution and frictional–viscous flow. *Nature Geoscience*, *10*(1), 51–57. https://doi.org/10.1038/ngeo2857

Fagereng, Å., & Sibson, R. H. (2010). Mélange rheology and seismic style. *Geology*, *38*(8), 751–754. https://doi.org/10.1130/G30868.1

Faulkner, D. R., Sanchez-Roa, C., Boulton, C., & den Hartog, S. A. M. (2017). Pore fluid pressure development in compacting fault gouge in theory, experiments, and nature. *Journal of Geophysical Research: Solid Earth*, *123*, 226–241. https://doi.org/10.1002/2017JB015130

Fisher, D., & Byrne, T. (1987). Structural evolution of underthrusted sediments. *Tectonics*, *6*(6), 775–793.

French, M. E., Chester, F. M., & Chester, J. S. (2015). Micromechanisms of creep in clay-rich gouge from the Central Deforming Zone of the San Andreas Fault. *Journal of Geophysical Research: Solid Earth*, *120*, 827–849. https://doi.org/10.1002/2014JB011496

Giorgetti, C., Carpenter, B. M., & Collettini, C. (2015). Frictional behavior of talc-calcite mixtures. *Journal of Geophysical Research: Solid Earth*, *120*, 6614–6633. https://doi.org/10.1002/2015JB011970.Received

Haines, S. H., Kaproth, B., Marone, C., Saffer, D., & Van Der Pluijm, B. (2013). Shear zones in clay-rich fault gouge: A laboratory study of fabric development and evolution. *Journal of Structural Geology*, *51*, 206–225. https://doi.org/10.1016/j.jsg.2013.01.002

Harris, R. N., Schierhorn, F. S., & Spinelli, G. (2011). Heat flow along the NanTroSEIZE transect: Results from IODP Expeditions 315 and 316 offshore the Kii Peninsula, Japan. *Geochemistry, Geophysics, Geosystems*, *12*, Q0AD16. https://doi.org/10.1029/2011GC003593

Hashimoto, Y., & Kimura, G. (1999). Underplating process from melange formation to duplexing: Example from the Cretaceous Shimanto Belt, Kii Peninsula, southwest Japan. *Tectonics*, *18*(1), 92–107. https://doi.org/10.1029/1998TC900014

Hawthorne, J. C., & Rubin, A. M. (2013). Laterally propagating slow slip events in a rate and state friction model with a velocity-weakening to velocity-strengthening transition. *Journal of Geophysical Research: Solid Earth*, *118*, 3785–3808. https://doi.org/10.1002/jgrb.50261

Hayman, N. W., & Lavier, L. L. (2014). The geologic record of deep episodic tremor and slip. *Geology*, *42*(3), 195–198. https://doi.org/10.1130/G34990.1

He, C., Luo, L., Hao, Q., & Zhou, Y. (2013). Velocity-weakening behavior of plagioclase and pyroxene gouges and stabilizing effect of small amounts of quartz under hydrothermal conditions. *Journal of Geophysical Research: Solid Earth*, *118*, 3408–3430. https://doi.org/10.1002/jgrb.50280

He, C., Wang, Z., & Yao, W. (2007). Frictional sliding of gabbro gouge under hydrothermal conditions. *Tectonophysics*, *445*, 353–362. https://doi.org/10.1016/j.tecto.2006.05.023

Heilbronner, R., & Keulen, N. (2006). Grain size and grain shape analysis of fault rocks. *Tectonophysics*, *427*, 199–216. https://doi.org/10.1016/j.tecto.2006.05.020

Hong, T., & Marone, C. (2005). Effects of normal stress perturbations on the frictional properties of simulated faults. *Geochemistry, Geophysics, Geosystems*, *6*, Q03012. https://doi.org/10.1029/2004GC000821

Humphris, S. E., & Thompson, G. (1977). Hydrothermal alteration of oceanic basalts by seawater. *Geochimica et Cosmochimica Acta*, *42*, 107–125.

Hyndman, R. D., Yamano, M., & Oleskevich, D. A. (1997). The seismogenic zone of subduction thrust faults. *Island Arc*, *6*, 244–260. https://doi.org/10.1785/gssrl.79.4.572

Ikari, M. J., Kopf, A. J., Hüpers, A., & Vogt, C. (2018). Lithologic control of frictional strength variations in subduction zone sediment inputs. *Geosphere*, *14*(2), 604–625. https://doi.org/10.1130/GES01546.1

Ikari, M. J., Marone, C., Saffer, D. M., & Kopf, A. J. (2013). Slip weakening as a mechanism for slow earthquakes. *Nature Geoscience*, *6*(6), 468–472. https://doi.org/10.1038/ngeo1818

Ikari, M. J., Saffer, D. M., & Marone, C. (2009). Frictional and hydrologic properties of clay-rich fault gouge. *Journal of Geophysical Research*, *114*, B05409. https://doi.org/10.1029/2008JB006089

Ikesawa, E., Kimura, G., Sato, K., Ikehara-Ohmori, K., Kitamura, Y., Yamaguchi, A., et al. (2005). Tectonic incorporation of the upper part of oceanic crust to overriding plate of a convergent margin: An example from the Cretaceous–early Tertiary Mugi Mélange, the Shimanto Belt, Japan. *Tectonophysics*, *401*, 217–230. https://doi.org/10.1016/j.tecto.2005.01.005

Kameda, J., Ujiie, K., Yamaguchi, A., & Kimura, G. (2011). Smectite to chlorite conversion by frictional heating along a subduction thrust. *Earth and Planetary Science Letters*, *305*(1–2), 161–170. https://doi.org/10.1016/j.epsl.2011.02.051

Kawabata, K., Tanaka, H., & Kimura, G. (2007). Mass transfer and pressure solution in deformed shale of accretionary complex: Examples from the Shimanto Belt, southwestern Japan. *Journal of Structural Geology*, *29*(4), 697–711. https://doi.org/10.1016/j.jsg.2006.11.009

Kawabata, K., Tanaka, H., Kitamura, Y., & Ma, K. F. (2009). Apparent activation energy and rate-limiting process estimation from natural shale deformed by pressure solution in shallow subduction zone. *Earth and Planetary Science Letters*, *287*(1–2), 57–63. https://doi.org/10.1016/j.epsl.2009.07.032

Keulen, N., Heilbronner, R., Stünitz, H., Boullier, A.-M., & Ito, H. (2007). Grain size distributions of fault rocks: A comparison between experimentally and naturally deformed granitoids. *Journal of Structural Geology*, *29*, 1282–1300. https://doi.org/10.1016/j.jsg.2007.04.003

Kimura, G., Yamaguchi, A., Hojo, M., Kitamura, Y., Kameda, J., Ujiie, K., et al. (2012). Tectonic mélange as fault rock of subduction plate boundary. *Tectonophysics*, *568–569*, 25–38. https://doi.org/10.1016/j.tecto.2011.08.025

Kitajima, H., & Saffer, D. M. (2012). Elevated pore pressure and anomalously low stress in regions of low frequency earthquakes along the Nankai Trough subduction megathrust. *Geophysical Research Letters*, *39*, L23301. https://doi.org/10.1029/2012GL053793

Kitamura, Y., Sato, K., Ikesawa, E., Ikehara-Ohmori, K., Kimura, G., Kondo, H., et al. (2005). Mélange and its seismogenic roof décollement: A plate boundary fault rock in the subduction zone—An example from the Shimanto Belt, Japan. *Tectonics*, *24*, TC5012. https://doi.org/10.1029/2004TC001635

Kohlstedt, D. L., Evans, B., & Mackwell, S. J. (1995). Strength of the lithosphere: Constraints imposed by laboratory experiments. *Journal of Geophysical Research*, *100*(B9), 17,587–17,602. https://doi.org/10.1029/95JB01460

Kotowski, A. J., & Behr, W. M. (2019). Length scales and types of heterogeneities along the deep subduction interface: Insights from exhumed rocks on Syros Island, Greece. *Geosphere*, *15*, 1–28. https://doi.org/10.1130/GES02037.1/4782963/ges02037.pdf

Landini, G. (2008), Advanced shape analysis with ImageJ, Proc. Second ImageJ User Dev. Conf., November, 116–121.

Leeman, J. R., Saffer, D. M., Scuderi, M. M., & Marone, C. (2016). Laboratory observations of slow earthquakes and the spectrum of tectonic fault slip modes. *Nature Communications*, *7*, 1–6. https://doi.org/10.1038/ncomms11104

Linker, M. F., & Dieterich, J. H. (1992). Effects of variable normal stress on rock friction: Observations and constitutive equations. *Journal of Geophysical Research*, *97*(B4), 4923–4940.

Liu, Y., & Rice, J. R. (2007). Spontaneous and triggered aseismic deformation transients in a subduction fault model. *Journal of Geophysical Research*, *112*, B09404. https://doi.org/10.1029/2007JB004930

Logan, J. M., Dengo, C. A., Higgs, N. G., & Wang, Z. Z. (1992). Fabrics of experimental fault zones: Their development and relationship to mechanical behavior. In B. Evans, & T. F. Wong (Eds.), *Fault Mechanics and Transport Properties of Rocks*, *International Geophysics*, (Vol. 51, edited by, pp. 33–67). Cambridge: Academic Press.

Logan, J. M., M. Friedman, N. Higgs, C. Dengo, and T. Shimamoto (1979), Experimental studies of simulated gouge and their application to studies of natural fault zones, *U. S. Geol. Surv. Open File Rep.*, (79–1239), 305–343.

Marone, C. (1998). Laboratory-derived friction laws and their application to seismic faulting. *Annual Review of Earth and Planetary Sciences*, *26*, 643–696. https://doi.org/10.1146/annurev.earth.26.1.643

Marone, C., Raleigh, C. B., & Scholz, C. H. (1990). Frictional behavior and constitutive modeling of simulated fault gouge. *Journal of Geophysical Research*, *95*(B5), 7007–7025.

Marone, C., & Scholz, C. H. (1988). The depth of seismic faulting and the upper transition from stable to unstable slip regimes. *Geophysical Research Letters*, *15*(6), 621–624.

Marone, C., & Scholz, C. H. (1989). Particle-size distribution and microstructures within simulated fault gouge. *Journal of Structural Geology*, *11*(7), 799–814. https://doi.org/10.1016/0191-8141(89)90099-0

Mavrommatis, A. P., Segall, P., & Johnson, K. M. (2014). A decadal-scale deformation transient prior to the 2011 M_w 9.0 Tohoku-oki earthquake. *Geophysical Research Letters*, *41*, 4486–4494. https://doi.org/10.1002/2014GL060139.Received

Mcguire, J. J., Collins, J. A., Davis, E., Becker, K., & Heesemann, M. (2018). A lack of dynamic triggering of slow slip and tremor indicates that the shallow Cascadia megathrust offshore Vancouver Island is likely locked. *Geophysical Research Letters*, *45*, 11,095–11,103. https://doi.org/10.1029/2018GL079519

Moore, G. F. Park, J.O., Bangs, N.L., Gulick, S.P., Tobin, H.J., Nakamura, Y., et al. (2009), Structural and seismic stratigraphic framework of the NanTroSEIZE Stage 1 transect, Proc. Integr. Ocean Drill. Progr., 314/315/31, 1–46, doi:https://doi.org/10.2204/iodp.proc.314315316.102.2009.

Moore, J. C. (1989). Tectonics and hydrogeology of accretionary prisms: Role of the decollement zone. *Journal of Structural Geology*, *11*(1/2), 95–106. https://doi.org/10.1016/0191-8141(89)90037-0

Moore, J. C., Rowe, C., & Meneghini, F. (2007). How accretionary prisms elucidate seismogenesis in subduction zones. In J. C. Moore, & T. H. Dixon (Eds.), *The Seismogenic Zone of Subduction Thrust Faults*, (pp. 288–315). New York, NY: Columbia University Press.

Moore, J. C., & Saffer, D. (2001). Updip limit of the seismogenic zone beneath the accretionary prism of southwest Japan: An effect of diagenetic to low-grade metamorphic processes and increasing effective stress. *Geology*, *29*(2), 183–186.

Nakano, M., Hori, T., Araki, E., Kodaira, S., & Ide, S. (2018). Shallow very-low-frequency earthquakes accompany slow slip events in the Nankai subduction zone. *Nature Communications*, *9*(1), 1–8. https://doi.org/10.1038/s41467-018-03431-5

Obana, K., & Kodaira, S. (2009). Low-frequency tremors associated with reverse faults in a shallow accretionary prism. *Earth and Planetary Science Letters*, *287*(1–2), 168–174. https://doi.org/10.1016/j.epsl.2009.08.005

Obana, K., Kodaira, S., Mochizuki, K., & Shinohara, M. (2001). Micro-seismicity around the seaward updip limit of the 1946 Nankai Earthquake dislocation area. *Journal of Geophysical Research*, *28*(12), 2333–2336.

Obara, K. (2002). Nonvolcanic deep tremor associated with subduction in southwest Japan. *Science*, *296*, 1679–1682.

Oleskevich, D. a., Hyndman, R. D., & Wang, K. (1999). The updip and downdip limits to great subduction earthquakes: Thermal and structural models of Cascadia, south Alaska, SW Japan, and Chile. *Journal of Geophysical Research*, *104*(B7), 14,965–14,991. https://doi.org/10.1029/1999JB900060

Perfettini, H., Schmittbuhl, J., Rice, J. R., & Cocco, M. (2001). Frictional response induced by time-dependent fluctuations of the normal loading. *Journal of Geophysical Research*, *106*(B7), 13,455–13,472.

Phillips, N. J., Rowe, C. D., & Ujiie, K. (2019). For how long are pseudotachylytes strong? Rapid alteration of basalt-hosted pseudotachylytes from a shallow subduction complex. *Earth and Planetary Science Letters*, *518*, 108–115. https://doi.org/10.1016/j.epsl.2019.04.033

Phillips, N. J., & White, J. C. (2017). Grain size-dependent strength of phyllosilicate-rich gouges in the shallow crust: Insights from the SAFOD site. *Journal of Geophysical Research: Solid Earth*, *122*, 1–24. https://doi.org/10.1002/2016JB013828

Poppe, L. J., V. F. Paskevich, J. C. Hathaway, and D. S. Blackwood (2001), A laboratory manual for X-ray powder diffraction, U.S. Geol. Surv. Open-File Rep. 01-041, 88.

Rabinowicz, E. (1951). The nature of the static and kinetic coefficients of friction. *Journal of Applied Physics*, *22*(11), 1373–1379. https://doi.org/10.1063/1.1699869

Rabinowicz, E. (1958). The intrinsic variables affecting the stick-slip process. *Proceedings of the Physical Society*, *71*, 668–675.

Rabinowitz, H. S., Savage, H. M., Skarbek, R. M., Ikari, M. J., Carpenter, B. M., & Collettini, C. (2018). Frictional behavior of input sediments to the Hikurangi Trench, New Zealand. *Geochemistry, Geophysics, Geosystems*, *19*, 1–18. https://doi.org/10.1029/2018GC007633

Reinen, L. A., & Weeks, J. D. (1993). Determination of rock friction constitutive parameters using an iterative least squares inversion method. *Journal of Geophysical Research*, *98*(B9), 15,937–15,950.

Rogers, G., & Dragert, H. (2003). Episodic tremor and slip on the Cascadia subduction zone: The chatter of silent slip. *Science*, *300*, 1942–1944.

Rowe, C. D., Moore, J. C., Meneghini, F., & McKeirnan, A. W. (2005). Large-scale pseudotachylytes and fluidized cataclasites from an ancient subduction thrust fault. *Geology*, *33*(12), 937–940. https://doi.org/10.1130/G21856.1

Rubin, A. M. (2008). Episodic slow slip events and rate-and-state friction. *Journal of Geophysical Research*, *113*, B11414. https://doi.org/10.1029/2008JB005642

Rubin, A. M., & Ampuero, J. (2005). Earthquake nucleation on (aging) rate and state faults. *Journal of Geophysical Research*, *110*, B11312. https://doi.org/10.1029/2005JB003686

Ruina, A. (1983). Slip instability and state variable friction laws. *Journal of Geophysical Research*, *88*(B12), 10,310–10,370.

Saffer, D. M., & Marone, C. (2003). Comparison of smectite- and illite-rich gouge frictional properties: Application to the updip limit of the seismogenic zone along subduction megathrusts. *Earth and Planetary Science Letters*, *215*(1–2), 219–235. https://doi.org/10.1016/S0012-821X(03)00424-2

Saffer, D. M., & Wallace, L. M. (2015). The frictional, hydrologic, metamorphic and thermal habitat of shallow slow earthquakes. *Nature Geoscience*, *8*(8), 594–600. https://doi.org/10.1038/ngeo2490

Sammis, C. G., & Ben-Zion, Y. (2008). Mechanics of grain-size reduction in fault zones. *Journal of Geophysical Research*, *113*, B02306. https://doi.org/10.1029/2006JB004892

Sammis, C. G., Osborne, R. H., Anderson, J. L., Banerdt, M., & White, P. (1986). Self-similar cataclasis in the formation of fault gouge. *Pure and Applied Geophysics*, *124*(1/2), 53–78.

Scholz, C. H. (1998). Earthquakes and friction laws. *Nature*, *391*, 37–42.

Scuderi, M. M., & Collettini, C. (2016). The role of fluid pressure in induced vs. triggered seismicity: Insights from rock deformation experiments on carbonates. *Scientific Reports*, *6*, 1, 24852–9. https://doi.org/10.1038/srep24852

Scuderi, M. M., Collettini, C., Viti, C., Tinti, E., & Marone, C. (2017). Evolution of shear fabric in granular fault gouge from stable sliding to stick slip and implications for fault slip mode. *Geology*, *45*(8), 731–734. https://doi.org/10.1130/G39033.1

Seyfried, W. E., & Bischoff, J. L. (1979). Low temperature basalt alteration by seawater: An experimental study at 70 °C and 150 °C. *Geochimica et Cosmochimica Acta*, *43*, 1937–1947.

Shelly, D. R., Beroza, G. C., & Ide, S. (2007). Non-volcanic tremor and low-frequency earthquake swarms. *Nature*, *446*(7133), 305–307. https://doi.org/10.1038/nature05666

Shibata, T., Orihashi, Y., Kimura, G., & Hashimoto, Y. (2008). Underplating of mélange evidenced by the depositional ages: U-Pb dating of zircons from the Shimanto accretionary complex, southwest Japan. *Island Arc*, *17*(3), 376–393. https://doi.org/10.1111/j.1440-1738.2008.00626.x

Sibson, R. H. (1982). Fault zone model, heat flow, and the depth distribution of earthquakes in the continental crust of the United States. *Bulletin of the Seismological Society of America*, *72*(1), 151–163.

Skarbek, R. M., Rempel, A. W., & Schmidt, D. A. (2012). Geologic heterogeneity can produce aseismic slip transients. *Geophysical Research Letters*, *39*, L21306. https://doi.org/10.1029/2012GL053762

Skarbek, R. M., & Savage, H. M. (2019). RSFit3000: A MATLAB GUI-based program for determining rate and state frictional parameters from experimental data. *Geosphere*, *15*(5), 1665–1676.

Sugihara, T., Kinoshita, M., Araki, E., Kimura, T., Kyo, M., Namba, Y., et al. (2014). Re-evaluation of temperature at the updip limit of locked portion of Nankai megasplay inferred from IODP Site C0002 temperature observatory. *Earth, Planets and Space*, *66*(107), 1–14.

Tembe, S., Lockner, D. A., & Wong, T. F. (2010). Effect of clay content and mineralogy on frictional sliding behavior of simulated gouges: Binary and ternary mixtures of quartz, illite, and montmorillonite. *Journal of Geophysical Research*, *115*, B03416. https://doi.org/10.1029/2009JB006383

Tonegawa, T., Araki, E., Kimura, T., Nakamura, T., Nakano, M., & Suzuki, K. (2017). Sporadic low-velocity volumes spatially correlate with shallow very low frequency earthquake clusters. *Nature Communications*, *8*(1), 1–7. https://doi.org/10.1038/s41467-017-02276-8

Uenishi, K., & Rice, J. R. (2003). Universal nucleation length for slip-weakening rupture instability under nonuniform fault loading. *Journal of Geophysical Research*, *108*(B1), 2042. https://doi.org/10.1029/2001JB001681

Ujiie, K., & Kimura, G. (2014). Earthquake faulting in subduction zones: Insights from fault rocks in accretionary prisms. *Progress in Earth and Planetary Science*, *1*(1), 7. https://doi.org/10.1186/2197-4284-1-7

Ujiie, K., Yamaguchi, A., Kimura, G., & Toh, S. (2007). Fluidization of granular material in a subduction thrust at seismogenic depths. *Earth and Planetary Science Letters*, *259*, 307–318. https://doi.org/10.1016/j.epsl.2007.04.049

Ujiie, K., Yamaguchi, H., Sakaguchi, A., & Toh, S. (2007). Pseudotachylytes in an ancient accretionary complex and implications for melt lubrication during subduction zone earthquakes. *Journal of Structural Geology*, *29*(4), 599–613. https://doi.org/10.1016/j.jsg.2006.10.012

Virkar, Y., & Clauset, A. (2014). Power-law distributions in binned empirical data. *The Annals of Applied Statistics*, *8*(1), 89–119. https://doi.org/10.1214/13-AOAS710

Wang, K., Hu, Y., & He, J. (2012). Deformation cycles of subduction earthquakes in a viscoelastic Earth. *Nature*, *484*, 327–332.

Wech, A. G., & Bartlow, N. M. (2014). Slip rate and tremor genesis in Cascadia. *Geophysical Research Letters*, *41*, 392–398. https://doi.org/10.1002/2014GL061184.Received

Williams, R. T., Farver, J. R., Onasch, C. M., Winslow, D. F., & Sio, A. (2015). An experimental investigation of the role of microfracture surfaces in controlling quartz precipitation rate: Applications to fault zone diagenesis Au Tube Diffusive Transport St. Peter Sand Reactant Substrate Interface (RSI). *Journal of Structural Geology*, *74*, 24–30. https://doi.org/10.1016/j.jsg.2015.02.011

Xing, T., Zhu, W., French, M., & Belzer, B. (2019). Stabilizing effect of high pore fluid pressure on slip behaviors of gouge-bearing faults. *Journal of Geophysical Research: Solid Earth*, *124*, 9526–9545. https://doi.org/10.1029/2019JB018002

Zhang, L., He, C., Liu, Y., & Lin, J. (2017). Frictional properties of the South China Sea oceanic basalt and implications for strength of the Manila subduction seismogenic zone. *Marine Geology*, *394*(December), 16–29. https://doi.org/10.1016/j.margeo.2017.05.006